Triple Phase-Shift Optimization of SiC-based Dual-Active Bridge DC/AC Converter

Adithyan Vetrivelan, Wei Xu, Ruiyang Yu, Alex Q. Huang
Semiconductor Power Electronics Center (SPEC)
Department of Electrical and Computer Engineering
University of Texas at Austin
Austin, Texas, USA

2022 IEEE Applied Power Electronics Conference and Exposition (APEC) | 978-1-6654-0688-8/22/$31.00 ©2022 IEEE | DOI: 10.1109/APEC43599.2022.9773574

***Abstract*—This paper presents a loss-optimized Triple Phase-Shift (TPS) switching strategy for Dual-Active Bridge (DAB) based converters. The proposed strategy considers minimizing total converter loss with respect to minimizing device rms currents, enabling Zero-Voltage Switching (ZVS) turn-on of devices and accurate control of device turn-off current. A model for switching currents is presented, followed by a loss model and optimization strategy. A 1.3*k*V/100*k*W prototype based on SiC MOSFETs was used in this work and experimental results up to 10*k*W show the proposed TPS strategy to be more efficient for operation.**

***Index Terms*—Dual-Active Bridge, Triple Phase-Shift, Wide Bang-Gap (WBG), Energy Storage, DC/AC**

I. Introduction

Dual-Active Bridge (DAB) based converters are gaining popularity for high-power DC/DC and DC/AC grid-tied applications due to attractive features namely, galvanic isolation, ZVS switching and bidirectional power transfer capability [1]–[3]. With the wider usage of Wide Band-Gap (WBG) devices which are capable of faster and more efficient switching, the aforementioned advantages of the DAB can be leveraged to realize more efficient converters.

Specific to DC/AC grid-tied applications, traditional solutions involve two stages: An isolated DC/DC stage followed by an inverter stage. This approach has two big drawbacks, namely: a large DC-link capacitance and switching losses in each stage. An alternate single-stage solution that is gaining popularity seeks to replace the second inverter stage with a simple line-frequency unfolding bridge [4]. This circuit is shown in fig. 1. The use of an unfolding bridge vastly reduces associated switching losses and also eliminates the need for a large DC-link capacitance, as the output voltage of the DC/DC stage will now follow the rectified AC grid voltage. In this case, the isolated DC/DC stage (DAB) will have to operate across a larger range of voltage and current. Efficient operation of the DAB stage is thus critical for system performance.

Many switching strategies have been proposed in literature for the DAB. The simplest method to control the DAB is through single-phase shift modulation (SPS) [5]. While SPS is acceptable at higher power levels [6], it suffers from high circulation currents which increases I^2R losses. Further, SPS is not favorable to ZVS when the DC/AC voltage gain is far from unity [7]. Other papers have proposed Dual Phase-Shift (DPS) [8], [9] and Triple Phase-Shift approaches [6], [10], [11]. Previously proposed TPS strategies suffer from complexity or only optimize for conduction loss and the DC/DC case.

The authors would like to credit the Solar Energy Technologies Office (SETO) of the U.S. Department of Energy for making this work possible.

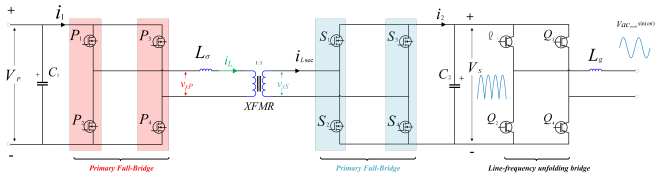

Fig. 1. DAB circuit with line-frequency unfolding bridge connection to grid

This paper proposes a complete model of the DAB switching currents as a function of all control parameters and an associated TPS optimization strategy which minimizes all losses in the converter. Section II briefly describes the DAB operation and reviews the conditions to achieve ZVS switching, and transformer limitations. Section III provides a detailed description of the relevant DAB operating modes and presents the model for switching currents and power as a function of the control parameters. Section IV presents the converter loss model and optimization strategy. The optimization results are presented for a real power case of 100*k*W, as well as the theoretical efficiency curve along the entire load range. Section V presents the experimental results for the proposed TPS switching strategy for the 10*k*W case and the results are compared with other switching strategies. Finally, Section VI summarizes the conclusions of this paper.

II. Dual-Active Bridge Operation and Control Parameters

Fig. 1 shows the DAB circuit with a line-frequency unfolding bridge connection to the AC grid. The DAB circuit consists of primary (DC side) and secondary (AC side) high-frequency full-bridges, a high-frequency transformer, an

energy transfer inductor L_σ and small DC-link capacitors. The primary switches (P_1 - P_4) and secondary switches (S_1 - S_4) are switched in such a way to produce a symmetrical quasi-square wave voltages $v_{xP}(t)$ and $v_{xS}(t)$ across the magnetic unit. $v_{xP}(t)$ and $v_{xS}(t)$ produce an inductor current $i_{Lpri}(t)$ and $i_{Lsec}(t)$ on the primary and secondary sides of the transformer respectively. For the circuit used here, the turns ratio of the transformer is 1:1 and hence for the remainder of this paper the inductor current will be simply referred to as $i_L(t)$. Capacitors C_1 and C_2 absorb the high-frequency components of the bridge current i_1 and i_2.

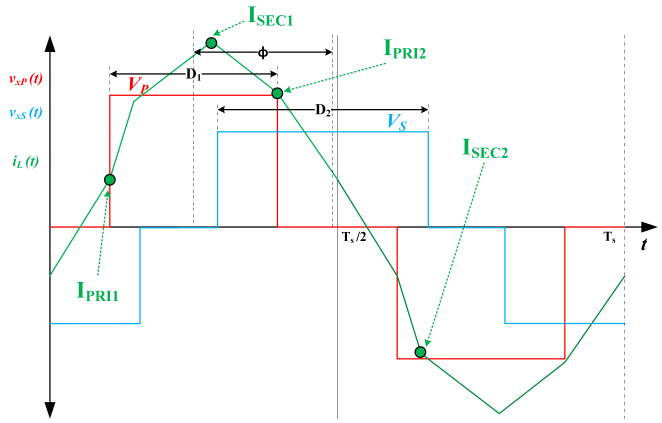

Fig. 2. DAB voltage and current waveforms over one switching cycle

The voltage and current waveforms of the DAB over one switching cycle are shown in fig. 2. For a given set of primary & secondary voltages (V_P and V_S) and L_σ, the power transfer through the DAB is controlled by four parameters, namely:

- D_1: the duty cycle of $v_{xP}(t)$, which can be a maximum of 50%
- D_2: the duty cycle of $v_{xS}(t)$, which can be a maximum of 50%
- ϕ: the phase shift between $v_{xP}(t)$ and $v_{xS}(t)$, which is between $-180° \leq \phi \leq +180°$
- f_s: the switching frequency of the bridges, which is usually determined by the frequency range of the magnetic components $f_{sMIN} \leq f_s \leq f_{sMAX}$

Of the listed control parameters, ϕ determines the direction of power transfer and from fundamental mode analysis it is easily seen that the power flow is from the leading voltage source to the lagging voltage source.

ZVS conditions for the DAB are well understood in literature [12], [13]. For the ideal ZVS condition where the charge across the discharging device is assumed to be zero, the ZVS conditions are summarized in (1).

$$I_{PRI1} < 0, I_{PRI2} > 0, I_{SEC1} > 0, I_{SEC2} < 0 \qquad (1)$$

where $I_{PRI1}, I_{PRI2}, I_{SEC1}, I_{SEC2}$ are the instantaneous inductor currents at the rising and falling edges of v_{xP} and v_{xS}, i.e. the switching currents. In the non-ideal case, the threshold value of 0 is replaced by the ZVS current required to achieve the complete discharge of the devices.

In the real DAB, peak value of the transformer current must be limited to prevent saturation of the magnetic core. This enforces an upper limit on the switching currents and is written as (2).

$$max[I_{PRI1}, I_{PRI2}, I_{SEC1}, I_{SEC2}] < I_{sat} \qquad (2)$$

where I_{sat} is the saturation current.

III. Operating Modes and Analysis

Previous papers [6] have identified twelve possible modes of operation for the DAB, as a function of the control parameters D_1, D_2, ϕ. Of these twelve, four modes are produced when $\phi \geq +90°$ or $\phi \leq -90°$. From fundamental mode analysis, it is understood that these modes are redundant since the peak of the power transfer occurs at $\phi = \pm 90°$. These extra modes increase inductor and device rms currents and produce more losses for the same power transfer capability. The eight remaining modes are labeled as $A - H$ in fig. 3 & fig. 4, and the control parameters conditions required to produce them are shown in (3). ϕ is normalized to $\pm 2\pi$ radians.

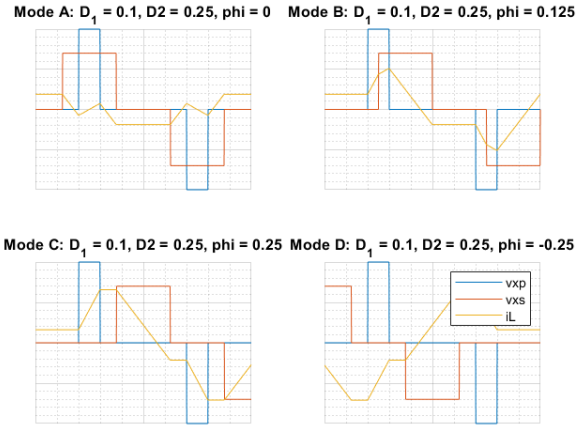

Fig. 3. DAB non-redundant modes of operation $A - D$. phi normalized to 2π.

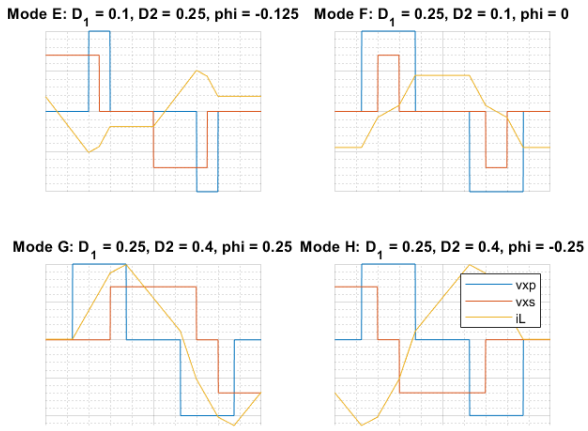

Fig. 4. DAB non-redundant modes of operation $E-H$. phi normalized to 2π.

$$\begin{cases} A & \text{if } \sigma_1 \le 0 \wedge \frac{D_1}{2} \le \frac{D_2}{2} + \phi \wedge \sigma_3 \le \frac{1}{2} \\ B & \text{if } 0 \le \sigma_1 \wedge \phi - \frac{D_2}{2} \le \frac{D_1}{2} \wedge \frac{D_1}{2} \le \frac{D_2}{2} + \phi \wedge \sigma_3 \le \frac{1}{2} \\ C & \text{if } \frac{D_1}{2} \le \phi - \frac{D_2}{2} \wedge \sigma_3 \le \frac{1}{2} \\ D & \text{if } \sigma_4 \le 0 \wedge \frac{D_1}{2} \le \sigma_2 \\ E & \text{if } 0 \le \sigma_4 \wedge \sigma_1 \le 0 \wedge \frac{D_2}{2} + \phi \le \frac{D_1}{2} \wedge \frac{D_1}{2} \le \sigma_2 \\ F & \text{if } 0 \le \sigma_1 \wedge \frac{D_2}{2} + \phi \le \frac{D_1}{2} \wedge \frac{D_1}{2} \le \sigma_2 \\ G & \text{if } 0 \le \sigma_1 \wedge \phi - \frac{D_2}{2} \le \frac{D_1}{2} \wedge \frac{1}{2} \le \sigma_3 \wedge \frac{D_2}{2} + \phi \le \frac{D_1}{2} + \frac{1}{2} \\ H & \text{if } 0 \le \sigma_4 \wedge \sigma_1 \le 0 \wedge \frac{D_2}{2} + \phi \le \frac{D_1}{2} \wedge \sigma_2 \le \frac{D_1}{2} \end{cases}$$

where

$$\begin{aligned} \sigma_1 &= D_1 - D_2 + 2\,\phi \\ \sigma_2 &= \phi - \tfrac{D_2}{2} + \tfrac{1}{2} \\ \sigma_3 &= \tfrac{D_1}{2} + \tfrac{D_2}{2} + \phi \\ \sigma_4 &= D_1 + D_2 + 2\,\phi \end{aligned} \tag{3}$$

A. Model for switching currents and DAB power

Table I shows the model developed in this work which specifies the switching currents I_1, I_2, I_3, I_4 as a function of the control parameters and circuit variables V_P, V_S, L_σ. These switching currents are reordered chronologically to get $I_{PRI1}, I_{PRI2}, I_{SEC1}, I_{SEC2}$ for all the modes $A-H$, using table II. Table III lists the equations for power transferred through the DAB for modes $A-H$.

IV. Loss Model and Optimization Strategy

A. Loss Model

The loss model used in this work considers the rms conduction losses in the devices and windings of the magnetic components, the switching losses associated with turn-on and turn-off of the SiC devices, and the core losses in the magnetic components. Since the TPS strategy does not affect losses in the line-frequency ($60Hz$) IGBT switching and conduction losses of the IGBT unfolding bridge, those losses are not presented here as part of the model used by the optimization strategy.

1) Conduction Losses: The conduction losses in the DAB are I^2R losses of the devices and the windings of the transformer and inductor.

a) Winding conduction losses: The inductor rms current I_{Lrms} (which is the same as the transformer rms current) can easily be calculated from the equations in [6]. The winding conduction loss $P_{cond,wind}$ can be calculated as (4):

$$P_{cond,wind} = I_{Lrms}^2 R_{wind} \tag{4}$$

b) Device conduction losses: Each of the devices on the primary bridge conduct the inductor current for half the switching cycle. The same is true for the devices on the secondary bridge. As a result, the device rms currents are proportional to the inductor rms currents and are given by (5).

$$I_{SiCrms} = \frac{I_{Lrms}}{\sqrt{2}} \tag{5}$$

and the subsequent device conduction losses $P_{cond,SiC}$ for the eight SiC switches are calculated as (6).

$$P_{cond,SiC} = 8\; I_{SiCrms}^2 R_{ds,ON} \tag{6}$$

The total conduction losses are given by (7)

$$P_{cond} = P_{cond,SiC} + P_{cond,wind} \tag{7}$$

2) Switching Losses:

a) Turn-on losses: As mention in Section II, (1) gives the ideal conditions for the DAB to achieve ZVS on all switching transitions. For the non-ideal case, the ZVS conditions are governed by (8) and the ZVS currents are calculated by (9).

$$\begin{aligned} I_{PRI1} &< -I_{ZVS,pri} \\ I_{PRI2} &> I_{ZVS,pri} \\ I_{SEC1} &> I_{ZVS,sec} \\ I_{SEC} &< -I_{ZVS,sec} \end{aligned} \tag{8}$$

$$\begin{aligned} I_{ZVS,pri} &= \sqrt{\frac{4\; E_{OSS,pri}}{L_\sigma}} \\ I_{ZVS,sec} &= \sqrt{\frac{4\; E_{OSS,sec}}{L_\sigma}} \end{aligned} \tag{9}$$

where $E_{OSS,pri}$ and $E_{OSS,sec}$ are the energies stored in the output capacitance of the devices on the primary and secondary bridges. For a given set of control parameters, the switching currents $I_{PRI1}, I_{PRI2}, I_{SEC1}, I_{SEC2}$ can be calculated from tables I and II. Combined with (9) and (8), the ZVS criteria can be evaluated for each transition in a switching cycle. If ZVS is achieved for all transitions, the turn-on energy is zero. For every transition that does not achieve

TABLE I
EQUATIONS FOR SWITCHING CURRENTS FOR MODES $A-H$ AS A FUNCTION OF CONTROL PARAMETERS

Mode	I_1	I_2	I_3	I_4
A	$-\frac{D_1\,\mathrm{Vp}-D_2\,\mathrm{Vs}}{2\,\mathrm{L}_\sigma\,\mathrm{fs}}$	$\frac{2\,\mathrm{Vs}\,\phi-D_1\,\mathrm{Vp}+D_1\,\mathrm{Vs}}{2\,\mathrm{L}_\sigma\,\mathrm{fs}}$	$\frac{2\,\mathrm{Vs}\,\phi+D_1\,\mathrm{Vp}-D_1\,\mathrm{Vs}}{2\,\mathrm{L}_\sigma\,\mathrm{fs}}$	$\frac{D_1\,\mathrm{Vp}-D_2\,\mathrm{Vs}}{2\,\mathrm{L}_\sigma\,\mathrm{fs}}$
B	$-\frac{D_1\,\mathrm{Vp}-D_2\,\mathrm{Vs}}{2\,\mathrm{L}_\sigma\,\mathrm{fs}}$	$\frac{2\,\mathrm{Vp}\,\phi-D_2\,\mathrm{Vp}+D_2\,\mathrm{Vs}}{2\,\mathrm{L}_\sigma\,\mathrm{fs}}$	$\frac{2\,\mathrm{Vs}\,\phi+D_1\,\mathrm{Vp}-D_1\,\mathrm{Vs}}{2\,\mathrm{L}_\sigma\,\mathrm{fs}}$	$\frac{D_1\,\mathrm{Vp}-D_2\,\mathrm{Vs}}{2\,\mathrm{L}_\sigma\,\mathrm{fs}}$
C	$-\frac{D_1\,\mathrm{Vp}-D_2\,\mathrm{Vs}}{2\,\mathrm{L}_\sigma\,\mathrm{fs}}$	$\frac{D_1\,\mathrm{Vp}+D_2\,\mathrm{Vs}}{2\,\mathrm{L}_\sigma\,\mathrm{fs}}$	$\frac{D_1\,\mathrm{Vp}-D_2\,\mathrm{Vs}}{2\,\mathrm{L}_\sigma\,\mathrm{fs}}$	$\frac{D_1\,\mathrm{Vp}-D_2\,\mathrm{Vs}}{2\,\mathrm{L}_\sigma\,\mathrm{fs}}$
D	$-\frac{D_1\,\mathrm{Vp}+D_2\,\mathrm{Vs}}{2\,\mathrm{L}_\sigma\,\mathrm{fs}}$	$\frac{D_1\,\mathrm{Vp}-D_2\,\mathrm{Vs}}{2\,\mathrm{L}_\sigma\,\mathrm{fs}}$	$\frac{D_1\,\mathrm{Vp}+D_2\,\mathrm{Vs}}{2\,\mathrm{L}_\sigma\,\mathrm{fs}}$	$\frac{D_1\,\mathrm{Vp}+D_2\,\mathrm{Vs}}{2\,\mathrm{L}_\sigma\,\mathrm{fs}}$
E	$-\frac{D_1\,\mathrm{Vp}-D_2\,\mathrm{Vs}}{2\,\mathrm{L}\sigma\,\mathrm{fs}}$	$\frac{2\,\mathrm{Vs}\,\phi-D_1\,\mathrm{Vp}+D_1\,\mathrm{Vs}}{2\,\mathrm{L}_\sigma\,\mathrm{fs}}$	$\frac{2\,\mathrm{Vp}\,\phi+D_2\,\mathrm{Vp}-D_2\,\mathrm{Vs}}{2\,\mathrm{L}_\sigma\,\mathrm{fs}}$	$\frac{2\,\mathrm{Vp}\,\phi+D_2\,\mathrm{Vp}-D_2\,\mathrm{Vs}}{2\,\mathrm{L}_\sigma\,\mathrm{fs}}$
F	$-\frac{D_1\,\mathrm{Vp}-D_2\,\mathrm{Vs}}{2\,\mathrm{L}_\sigma\,\mathrm{fs}}$	$\frac{2\,\mathrm{Vp}\,\phi-D_2\,\mathrm{Vp}+D_2\,\mathrm{Vs}}{2\,\mathrm{L}_\sigma\,\mathrm{fs}}$	$\frac{2\,\mathrm{Vp}\,\phi+D_2\,\mathrm{Vp}-D_2\,\mathrm{Vs}}{2\,\mathrm{L}_\sigma\,\mathrm{fs}}$	$\frac{2\,\mathrm{Vp}\,\phi+D_2\,\mathrm{Vp}-D_2\,\mathrm{Vs}}{2\,\mathrm{L}_\sigma\,\mathrm{fs}}$
G	$\frac{2\,\mathrm{Vs}\,\phi+D_1\,\mathrm{Vp}-D_1\,\mathrm{Vs}}{2\,\mathrm{L}_\sigma\,\mathrm{fs}}$	$\frac{2\,\mathrm{Vs}\,\phi-\mathrm{Vs}+D_1\,\mathrm{Vp}+D_1\,\mathrm{Vs}}{2\,\mathrm{L}_\sigma\,\mathrm{fs}}$	$-\frac{2\,\mathrm{Vp}\,\phi-\mathrm{Vp}+D_2\,\mathrm{Vp}+D_2\,\mathrm{Vs}}{2\,\mathrm{L}_\sigma\,\mathrm{fs}}$	$-\frac{2\,\mathrm{Vp}\,\phi-D_2\,\mathrm{Vp}+D_2\,\mathrm{Vs}}{2\,\mathrm{L}_\sigma\,\mathrm{fs}}$
H	$\frac{2\,\mathrm{Vs}\,\phi-D_1\,\mathrm{Vp}+D_1\,\mathrm{Vs}}{2\,\mathrm{L}_\sigma\,\mathrm{fs}}$	$\frac{2\,\mathrm{Vp}\,\phi+D_2\,\mathrm{Vp}-D_2\,\mathrm{Vs}}{2\,\mathrm{L}_\sigma\,\mathrm{fs}}$	$\frac{\mathrm{Vp}+2\,\mathrm{Vp}\,\phi-D_2\,\mathrm{Vp}-D_2\,\mathrm{Vs}}{2\,\mathrm{L}_\sigma\,\mathrm{fs}}$	$-\frac{\mathrm{Vs}+2\,\mathrm{Vs}\,\phi-D_1\,\mathrm{Vp}-D_1\,\mathrm{Vs}}{2\,\mathrm{L}_\sigma\,\mathrm{fs}}$

TABLE II
SWITCHING CURRENTS $I_{PRI1}, I_{PRI2}, I_{SEC1}, I_{SEC2}$ FOR MODES $A-H$ AS A FUNCTION OF I_1, I_2, I_3, I_4

M	I_{PRI1}	I_{PRI2}	I_{SEC1}	I_{SEC2}
A	I_2	I_3	I_1	$-I_1$
B	I_1	I_3	I_2	$-I_1$
C	I_1	I_2	I_2	I_3
D	I_1	I_2	$-I_2$	I_1
E	I_2	$-I_1$	I_1	I_3
F	I_1	$-I_1$	I_2	I_3
G	$-I_2$	I_1	$-I_4$	I_3
H	I_1	I_4	$-I_3$	I_2

TABLE III
EQUATIONS FPR P_{DAB} FOR MODES $A-H$ AS A FUNCTION OF CONTROL PARAMETERS

M	P_{DAB}
A	$\frac{2V_PV_SD_1\phi}{2\pi f_sL_\sigma}$
B	$\frac{2\pi V_PV_S\left[D_1D_2-\frac{1}{4}\left(\frac{\phi}{\pi}-(D_1+D_2)\right)^2\right]}{2\pi f_sL_\sigma}$
C	$\frac{2V_PV_SD_1D_2}{2f_sL_\sigma}$
D	$-\frac{2V_PV_SD_1D_2}{2f_sL_\sigma}$
E	$-\frac{2\pi V_PV_S\left[D_1D_2-\frac{1}{4}\left(\frac{\phi}{\pi}+(D_1+D_2)\right)^2\right]}{2\pi f_sL_\sigma}$
F	$\frac{2V_PV_SD_2\phi}{2\pi f_sL_\sigma}$
G	$-\frac{\pi V_PV_S\left[(\frac{\phi}{\pi}-\frac{1}{2})^2+\frac{1}{4}-D_1(1-D_1)-D_2(1-D_2)\right]}{2\pi f_sL_\sigma}$
H	$\frac{\pi V_PV_S\left[(\frac{\phi}{\pi}+\frac{1}{2})^2+\frac{1}{4}-D_1(1-D_1)-D_2(1-D_2)\right]}{2\pi f_sL_\sigma}$

ZVS, the turn-on loss $P_{turn-on}$ is increased by $2E_{ON}f_s$. Equations (10), (11) and (12) are used to calculate turn-on losses in the DAB.

$$P_{turn-on,pri}=\sum_{i=1}^{2}\begin{matrix}0,\text{if ZVS}\\2E_{ON,pri}f_s,\text{if no ZVS}\end{matrix} \tag{10}$$

$$P_{turn-on,sec}=\sum_{i=1}^{2}\begin{matrix}0,\text{if ZVS}\\2E_{ON,sec}f_s,\text{if no ZVS}\end{matrix} \tag{11}$$

$$P_{turn-on}=P_{turn-on,pri}+P_{turn-on,sec} \tag{12}$$

b) Turn-off losses: Similar to the turn-on losses, the turn-off losses also use the switching currents $I_{PRI1}, I_{PRI2}, I_{SEC1}, I_{SEC2}$. The turn-off losses can be modeled as an exponential function of the turn-off current from the datasheet of the SiC device.

$$P_{turn-off}=f(I_{PRI1}, I_{PRI2}, I_{SEC1}, I_{SEC2}) \tag{13}$$

3) Core losses: The core losses in the transformer and inductor are modeled using the Steinmetz's equation (14).

$$P_{core}=Kf_s^{\alpha}B^{\beta} \tag{14}$$

B. Optimization Strategy

Fig. 5 summarizes the optimization strategy proposed in this paper. The strategy is as follows: With the circuit variables V_P, V_S, L_σ and the power command P known, the required instantaneous power and current at a given point in the line-cycle is calculated. Depending on these requirements, the set of feasible modes M_F is determined. The optimization algorithm then iterates through operating points in these feasible modes and using the equations in table I, evaluates $I_{PRI1}, I_{PRI2}, I_{SEC1}, I_{SEC2}$, along with i_{Lrms}. Using these evaluated switching currents and rms currents, the loss model is employed to calculated the total converter loss. The optimization algorithm thus arrives at a single operating point which minimizes converter loss at a given point in the line-cycle for DC/AC case. This process is repeated for all unique operating points in the line-cycle.

The loss model presented in section IV part A evaluates the turn-on losses subject to ZVS constraints but the algorithm does not enforce ZVS switching. At some points, the algorithm may sacrifice ZVS in favor of reduced overall loss. During the execution of the algorithm, the maximum of the switching currents is checked to ensure that the constraint of (2) is satisfied.

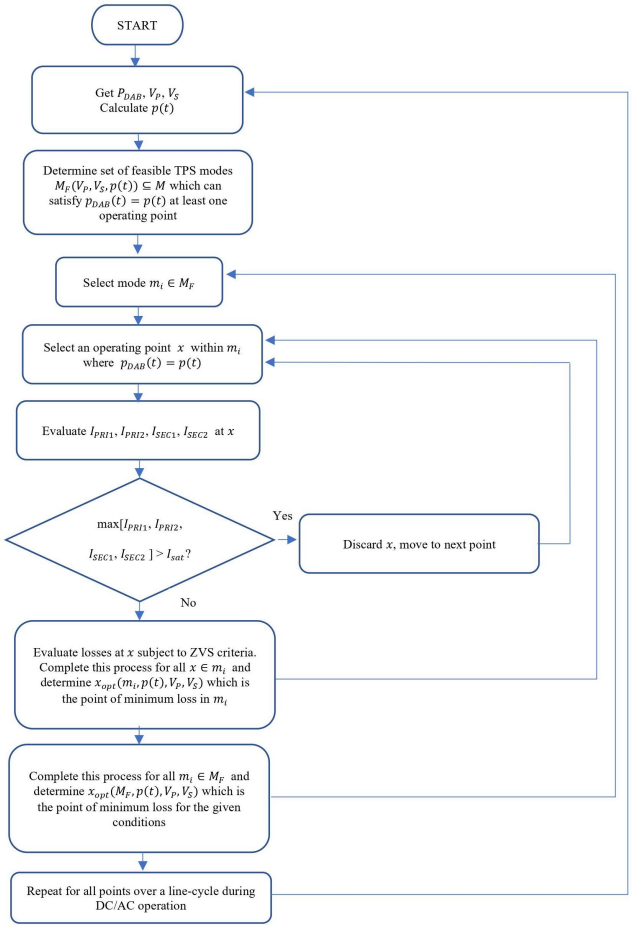

Fig. 5. TPS optimization strategy

1) Optimization for real power case of 100 kW: The optimization strategy was performed for a 100kW DC/AC case and the results are shown here. The input voltage was set to 1000VDC, and the AC voltage was set to 1200Vacpeak (850Vrms). The switching frequency was fixed at 15kHz. Fig. 6 and fig. 7 show the variation of the control parameters and converters losses over the line-cycle. ϕ here has been normalized to 2π and hence the range of acceptable value is $-0.25 \leq \phi_{pu} \leq +0.25$, corresponding to $-90° \leq \phi \leq +90°$.

The regions of the line-cycle that achieve ZVS are shown in fig. 8 and fig. 9. ZVS conditions are evaluated as per (8) and (9). As seen, ZVS is achieved in this case at almost all points over the AC half line-cycle.

Finally, the theoretical converter efficiency over the complete load range is shown in fig. 10. As seen, the maximum efficiency can reach almost 99%.

V. Experimental Results

The TPS optimization strategy proposed in this paper was implemented and the converter was tested up to 10kW under three conditions: A) Voltage gain 0.5 ($R_{LOAD} = 2.2\Omega$), B) Voltage gain unity ($R_{LOAD} = 23.4\Omega$) (low-power case), and

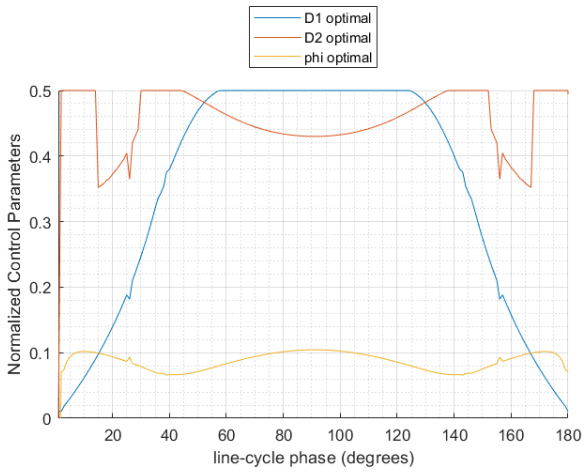

Fig. 6. Variation of control parameters D_1, D_2, ϕ_{pu} along an AC half line-cycle with $V_P = 1000VDC$ and $V_S = 1200Vacpeak(850Vrms)$

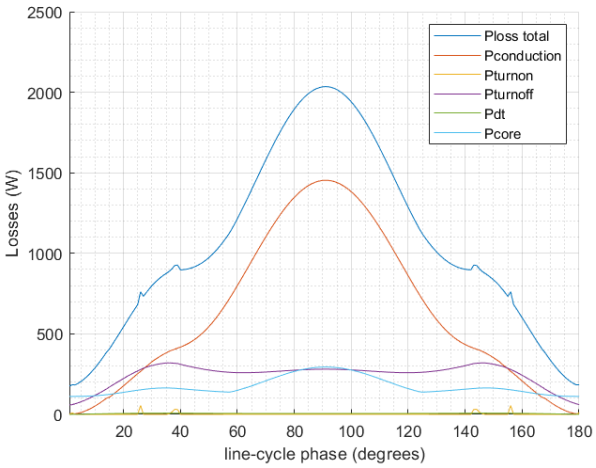

Fig. 7. Loss Breakdown for a 100kW case over an AC half line-cycle with $V_P = 1000VDC$ and $V_S = 1200Vacpeak(850Vrms)$

C) Voltage gain unity ($R_{LOAD} = 9.4\Omega$) (high-power case). Converter efficiency was measured using a HIOKI PW6001 power analyzer. The efficiency was recorded for the TPS case and compared with alternative switching strategies. It is observed that the TPS strategy results in superior performance.

A. Voltage gain 0.5 ($R_{LOAD} = 2.2\Omega$)

Fig. 11 and fig. 12 show the 10kW experimental results for case where the output AC voltage is close to half the DC input voltage. The input voltage V_P is set to $430VDC$, and the load resistance $R_{LOAD} = 2.2\Omega$. Fig. 11 implements the proposed TPS strategy and fig. 12 implements a single-phase shift variable-frequency (SPS VF) strategy. The associated efficiency curves are shown in fig. 13 and it is observed that the TPS strategy shows superior efficiency. This is mainly attributed to the reduced switching currents in the TPS case

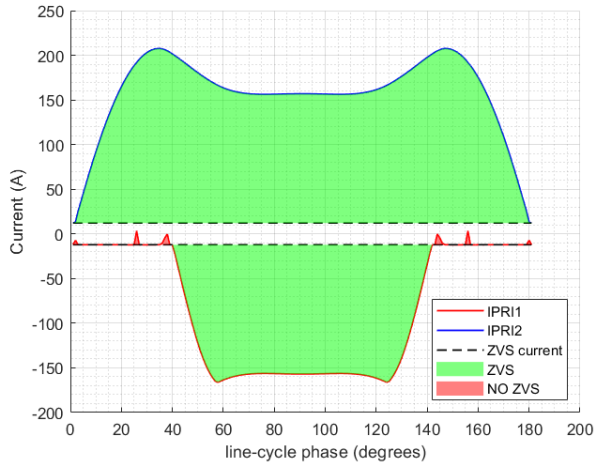

Fig. 8. ZVS region for primary switches over the AC half line-cycle

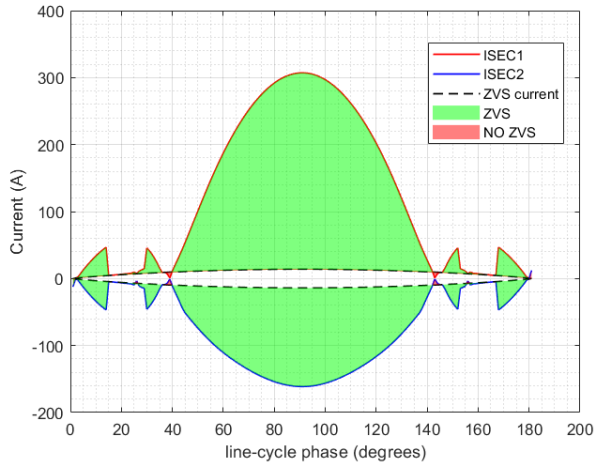

Fig. 9. ZVS region for secondary switches over the AC half line-cycle

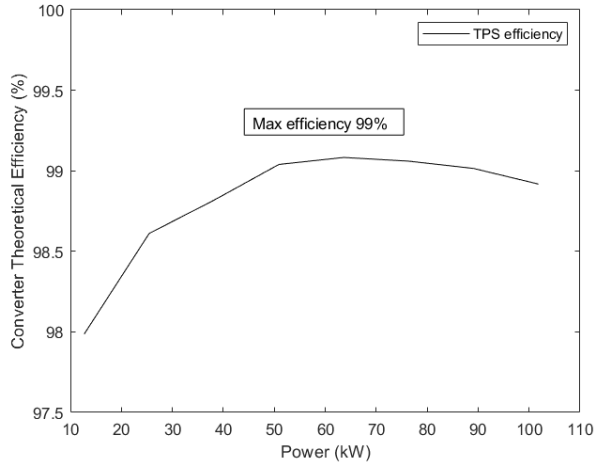

Fig. 10. Theoretical converter efficiency over the complete load range using TPS

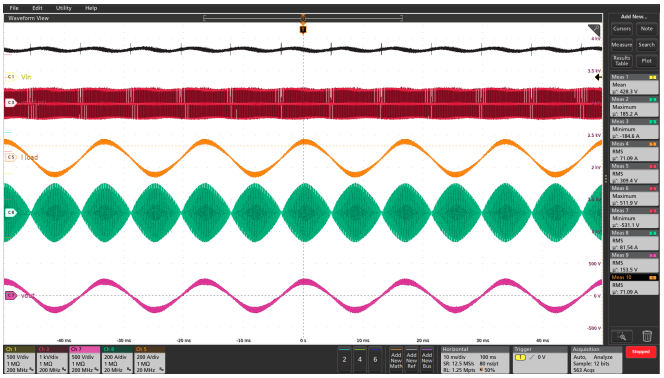

Fig. 11. Waveforms for TPS switching strategy, voltage gain close to 0.5 ($R_{LOAD} = 2.2\Omega$). Top to bottom: $V_P = 430VDC$, v_{xP}, load current = $70Arms$, i_L, $V_S = 152Vrms$ (load voltage)

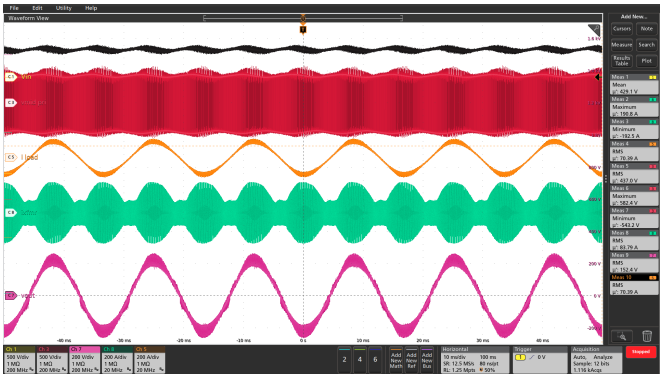

Fig. 12. Waveforms for SPS VF switching strategy, voltage gain close to 0.5 ($R_{LOAD} = 2.2\Omega$). Top to bottom: $V_P = 430VDC$, v_{xP}, load current = $70Arms$, i_L, $V_S = 152Vrms$ (load voltage)

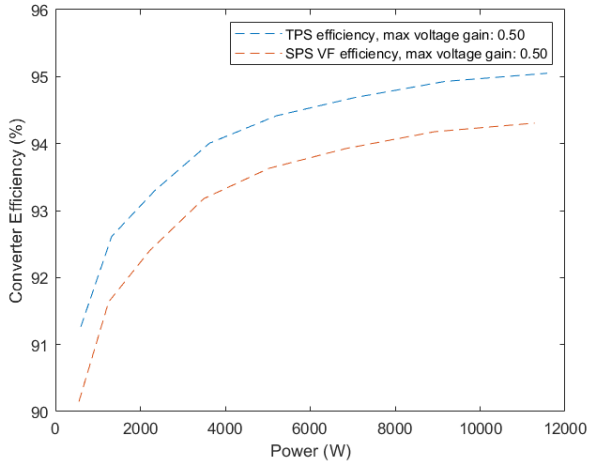

Fig. 13. Efficiency comparison between and TPS and SPS VF switching strategy for voltage gain close to 0.5

as seen from the envelope of i_L in the waveforms.

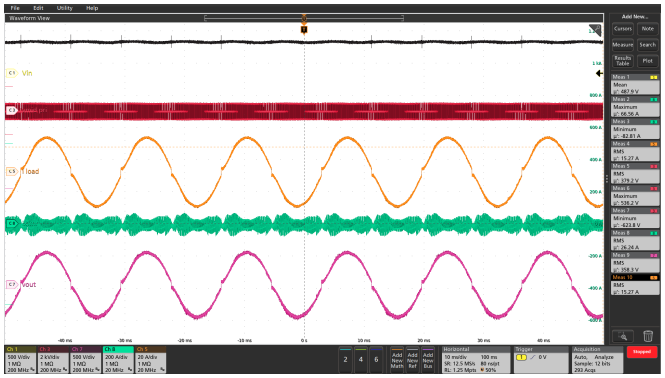

Fig. 14. Waveforms for TPS switching strategy, voltage gain close to unity ($R_{LOAD} = 23.4\Omega$). Top to bottom: $V_P = 488VDC$, v_{xP}, load current = $15Arms$, i_L, $V_S = 358Vrms$ (load voltage)

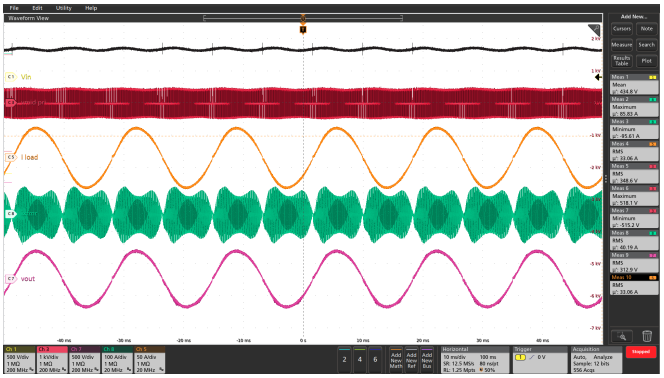

Fig. 16. Waveforms for TPS switching strategy, voltage gain close to unity. Top to bottom: $V_P = 435VDC$, v_{xP}, load current = $33Arms$, i_L, $V_S = 313Vrms$ (load voltage)

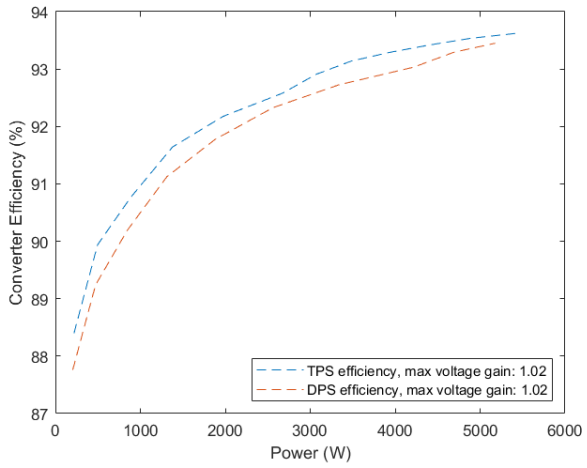

Fig. 15. Efficiency comparison between TPS and DPS switching strategy for voltage gain close to unity (low-power case)

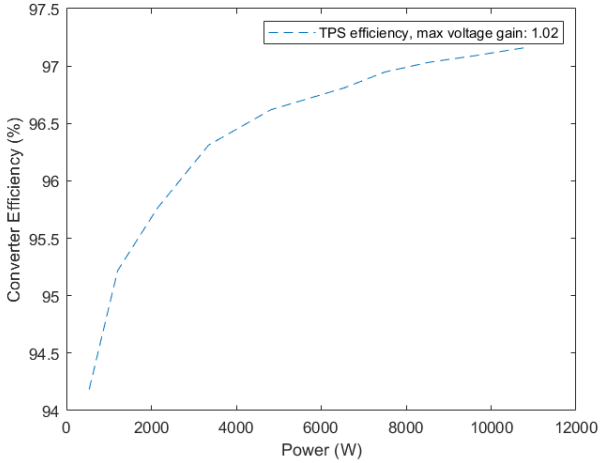

Fig. 17. Efficiency of TPS switching strategy for voltage gain close to unity (high-power case)

B. Voltage gain unity ($R_{LOAD} = 23.4\Omega$) (low-power case)

Fig. 14 shows the 6kW experimental results for case where the output AC voltage is close to the DC input voltage. The input voltage V_P is set to $488VDC$, and the load resistance $R_{LOAD} = 23.4\Omega$. Fig. 14 implements the proposed TPS strategy, and the same test was also run with a Dual Phase-Shift (DPS) strategy. The associated efficiency curves are shown in fig. 15 and it is observed that the TPS strategy shows superior efficiency.

C. Voltage gain unity ($R_{LOAD} = 9.4\Omega$) (high-power case)

The DAB is generally suited for higher efficiency when operating around unity voltage gain. Fig. 16 shows the implementation of the TPS strategy for the 10kW case with the output AC close to the input voltage. The input voltage V_P is set to $488VDC$, and the load resistance $R_{LOAD} = 9.4\Omega$. Fig. 17 shows the associated efficiency curve. As seen, the efficiency achieved is easily above 97%. In this high-power region, the TPS and DPS strategies converge to the same efficiency.

VI. Conclusion

The complete model of the Dual-Active Bridge (DAB) switching currents presented in this work and the associated Triple Phase-Shift (TPS) optimization strategy can enable highly efficient operation of the DAB across a range of voltages and currents. The experimental waveforms and efficiency curves were shown for a range of powers and voltage gains, and compared with other popular switching strategies. It is seen that the Triple Phase-Shift switching strategy results in superior efficiency or efficiency equal to that of the next-best switching strategy.

References

[1] B. Zhao, Q. Song, W. Liu and Y. Sun, "Overview of Dual-Active-Bridge Isolated Bidirectional DC–DC Converter for High-Frequency-Link Power-Conversion System," in IEEE Transactions on Power Electronics, vol. 29, no. 8, pp. 4091-4106, Aug. 2014, doi: 10.1109/TPEL.2013.2289913

[2] B. Zhao, Q. Yu and W. Sun, "Extended-Phase-Shift Control of Isolated Bidirectional DC–DC Converter for Power Distribution in Microgrid," in IEEE Transactions on Power Electronics, vol. 27, no. 11, pp. 4667-4680, Nov. 2012, doi: 10.1109/TPEL.2011.2180928.
[3] F. Krismer and J. W. Kolar, "Accurate Power Loss Model Derivation of a High-Current Dual Active Bridge Converter for an Automotive Application," in IEEE Transactions on Industrial Electronics, vol. 57, no. 3, pp. 881-891, March 2010, doi: 10.1109/TIE.2009.2025284.
[4] W. Xu, Z. Guo, A. Vetrivelan, R. Yu and A. Q. Huang, "Hardware Design of a 13.8kV/3MVA PV Plus Storage Solid State Transformer (PVS-SST)," in IEEE Journal of Emerging and Selected Topics in Power Electronics, doi: 10.1109/JESTPE.2021.3082033.
[5] M. N. Kheraluwala, R. W. Gascoigne, D. M. Divan and E. D. Baumann, "Performance characterization of a high-power dual active bridge DC-to-DC converter," in IEEE Transactions on Industry Applications, vol. 28, no. 6, pp. 1294-1301, Nov.-Dec. 1992, doi: 10.1109/28.175280.
[6] F. Krismer and J. W. Kolar, "Closed Form Solution for Minimum Conduction Loss Modulation of DAB Converters," in IEEE Transactions on Power Electronics, vol. 27, no. 1, pp. 174-188, Jan. 2012, doi: 10.1109/TPEL.2011.2157976.
[7] W. Xu et al., "Hardware Design and Demonstration of a 100kW, 99% Efficiency Dual Active Half Bridge Converter Based on 1700V SiC Power MOSFET," 2020 IEEE Applied Power Electronics Conference and Exposition (APEC), 2020, pp. 1367-1373, doi: 10.1109/APEC39645.2020.9124401.
[8] F. Jauch and J. Biela, "Single-phase single-stage bidirectional isolated ZVS AC-DC converter with PFC," 2012 15th International Power Electronics and Motion Control Conference (EPE/PEMC), 2012, pp. LS5d.1-1-LS5d.1-8, doi: 10.1109/EPEPEMC.2012.6397479.
[9] T. Chen, R. Yu, Q. Huang and A. Q. Huang, "A single-stage bidirectional dual-active-bridge AC-DC converter based on enhancement mode GaN power transistor," 2018 IEEE Applied Power Electronics Conference and Exposition (APEC), 2018, pp. 723-728, doi: 10.1109/APEC.2018.8341092.
[10] S. S. Shah and S. Bhattacharya, "A Simple Unified Model for Generic Operation of Dual Active Bridge Converter," in IEEE Transactions on Industrial Electronics, vol. 66, no. 5, pp. 3486-3495, May 2019, doi: 10.1109/TIE.2018.2850012.
[11] J. Huang, Y. Wang, Z. Li and W. Lei, "Unified Triple-Phase-Shift Control to Minimize Current Stress and Achieve Full Soft-Switching of Isolated Bidirectional DC–DC Converter," in IEEE Transactions on Industrial Electronics, vol. 63, no. 7, pp. 4169-4179, July 2016, doi: 10.1109/TIE.2016.2543182.
[12] J. Everts, "Closed-Form Solution for Efficient ZVS Modulation of DAB Converters," in IEEE Transactions on Power Electronics, vol. 32, no. 10, pp. 7561-7576, Oct. 2017, doi: 10.1109/TPEL.2016.2633507.
[13] Wei Xu, Rui yang Yu, Zhicheng Guo, Alex Q. Huang, "Design of 1500V/200kW 99.6% Efficiency Dual Active Bridge Converters Based on 1700V SiC Power MOSFET Module", 2020 IEEE Energy Conversion Congress and Exposition (ECCE), Detroit, MI, USA, in press